Advanced Materials Science and Technology Vol 6 Issue 1 2024
DOI: 10.37155/2717–526X–0601–2

ORIGINAL RESEARCH ARTICLE

Open Access

Omniscient Pte.Ltd.

Structural Modification of Partially Ni-substituted MnHCF Cathode Material for Aqueous Zn-ion Batteries

Mariam Maisuradze[1], Min Li[1], Mattia Gaboardi[2], Giuliana Aquilanti[2], Jasper Rikkert Plaisier[2], Marco Giorgetti[1*]

[1]Department of Industrial Chemistry "Toso Montanari", University of Bologna, Bologna 40136, Italy.
[2]Elettra Sincrotrone Trieste, Trieste 34149, Italy.

***Correspondence to:** Marco Giorgetti, Department of Industrial Chemistry "Toso Montanari", University of Bologna, Viale Risorgimento 4, Bologna 40136, Italy. Email: marco.giorgetti@unibo.it

Received: March 3, 2024; **Accepted:** April 3, 2024; **Published Online:** April 9, 2024

Citation: Maisuradze M, Li M, Gaboardi M, Aquilanti G, Plaisier JR and Giorgetti M. Structural Modification of Partially Ni-substituted MnHCF Cathode Material for Aqueous Zn-ion Batteries. *Advanced Materials Science and Technology*, 2024;6(1):0629615. https://doi.org/10.37155/2717-526X-0601-2

Abstract: The initial capacity fading and electrochemical profile modification of the nickel substituted manganese hexacyanoferrate cathode material in aqueous zinc-ion batteries was investigated. The outcome of the electrochemical tests suggested the structural transformation of the material; therefore, further characterization has been performed with the synchrotron-based x-ray absorption spectroscopy and powder x-ray diffraction. Indeed, the alteration of the structure was evident with both techniques. The dissolution of Mn and Ni was observed, alongside with the substitution of Mn with Zn. Furthermore, a new Zn-containing phase formation, and the modification of Mn species were demonstrated.

Keywords: Aqueous batteries; Zn-ion batteries; X-ray absorption spectroscopy; X-ray diffraction; Operando measurement; Manganese hexacyanoferrate

1. Introduction

Nowadays, with the increasing world population and rapid technological advancements, energy consumption is constantly rising. Therefore, the progress must be made in the associated energy production and storage fields, which is a complex and challenging task. Batteries, especially secondary, or rechargeable batteries, are one of the main players of the energy storage devices. Even though, the Li-ion batteries (LIBs) are still dominating in the rechargeable battery market, post-LIBs are attracting more and more attention. For the development of the new systems, the thorough investigation of each component and the deep understanding of the electrochemical mechanism is necessary. Indeed, the progress is made, even leading to the commercialization of the first Na-ion batteries

(SIBs) by Contemporary Amperex Technology Co., Ltd., based on the Prussian White cathode material, from the family of the Prussian Blue Analogue (PBA)[1].

SIBs are not the only perspective substitution for LIBs, the research is actively conducting on potassium, calcium, magnesium, zinc etc. This work is focusing on zinc-ion batteries (ZIBs), namely in aqueous battery systems (AZIBs). AZIBs attracted interest towards them, due to the advantages of both, as an aqueous electrolyte, and Zn metal as an electrode[2-4]. The main advantages of zinc are its low cost, nontoxicity, high theoretical gravimetric (820 mAh • g^{-1}) and volumetric capacity (5855 mAh • cm^{-3}), and low standard reduction potential (-0.76 V *vs*. SHE)[3]. On the other hand, moving to the aqueous media, gives the opportunity of avoiding highly toxic and flammable organic solvents, which generally have higher fabrication costs and two orders of magnitude lower ionic conductivities, than their aqueous counterparts.

The cathode material of interest in this study is partially nickel substituted manganese hexacyanoferrate, which is from the same PBA family, as aforementioned, newly commercialized Prussian White for SIBs. Prussian Blue (PB) and its analogues are large family of transition metal hexacyanoferrates, with general formula of $A_xM[Fe(CN)_6]_\gamma\square_{1-\gamma} \bullet zH_2O$, where A is an alkali metal such as Li^+, Na^+, K^+, *etc*.; M is transition metal ions: Fe, Co, Mn, Ni, Cu, *etc*.; □ is a vacancy; $0 < x < 2$; $0 < y < 1$[5]. They contain open ionic channels, leading to the higher diffusion coefficient of 10^{-9} $cm^2 \bullet s^{-1}$ to 10^{-8} $cm^2 \bullet s^{-1}$[6,7], and consequently higher ionic conductivity. Also, the PBA lattice, due to its robust and large 3D channel frameworks, is structurally and dimensionally stable, with almost zero lattice strain[8] towards the insertion and extraction processes[5]. Therefore, PBAs have been widely used as electrode material for Li-ion and post-Li-ion batteries[9-17].

Generally, both redox centers $M^{+2/+3}$ and $Fe^{+2/+3}$ of PBAs can be (but not necessarily) electroactive, which means two electron redox capacity and consequently two alkali ion storage. The first reported work about the implementation of PBAs in AZIBs was in 2015 by Jia *et al*.[18], demonstrating reversible insertion of Zn^{2+} ions in copper hexacyanoferrate (CuHCF) nano-cubes.

Among simple PBAs, manganese hexacyanoferrate (MnHCF) has attracted much interest[19], in terms of sustainability, safety, cost-effectiveness, abundance and non-toxicity. Also, large specific capacity derived from the two active redox couples (Fe^{3+}/Fe^{2+} and Mn^{3+}/Mn^{2+}), and the relatively high discharge voltage are attractive qualities for the cathode material. However, MnHCF in AZIBs displayed severe dissolution, forming a new Zn-containing phase[20-22]. One of the main reasons is believed to be the severe crystal Jahn-Teller (JT) distortion effect, which Mn^{III} compounds are subjected to. The removal of one of the electrons from the e_g orbital of d^5 Mn^{2+} HS[23] leads to the basal plane shrinkage[24], and different orbital distribution, the d_z^2 being less perturbed by the potential generated by the cyanides, than the $d_{x^2-y^2}$.

Generally, the properties of PBAs can be changed by heteroatom doping or partial substitution of the high spin ions, which can help to adjust the electrochemical properties by providing the additional degree of freedom. Some of the examples are iron[25], cobalt[26], and nickel[27,28], as they are reported to help with relaxing the Jahn-Teller distortion in MnHCF. The atomic radius of the latter one is almost equal to the atomic radius of Mn, therefore, when the Ni replaces the Mn inside the PBA structure, the cubic framework remains in a good order. It is generally known that, during the insertion/extraction process, the Ni sites are unreactive and they are just balancing the tiny structural disturbances caused by the redox reactions on the Mn sites[28,29]. The synthesis and advanced characterization of the 10% Ni-substituted MnHCF (hereby referred as NiMnHCF) has been already described in previous works [30].

Advanced x-ray techniques are among the most sophisticated characterisation methods in the battery material research. The x-ray absorption spectroscopy (XAS) provides the profound understanding about the oxidation states of the elements, their coordination and nearest neighbourhood. For cathode material XAS can help to determine the electrochemical activity of metals and their local structure; it can follow the modification of the elemental species, and identify them.

The powder x-ray diffraction (PXRD) probes the long-range structure of the material, describing the crystallinity, symmetry, unit cell parameters and phase modification, that can be extremely helpful for the characterization of the battery materials and for following the alterations inside the structure during the aging process. Especially, in *operando* modality,

PXRD measurement provides the possibility to analyze the cathode during the operational conditions, which is extremely important for the understanding the true dynamics of the system, and being able to follow the gradual structural modifications inside the electrode, giving additional time-resolution to the structural investigation.

In this work, we followed the electrochemical behavior of the NiMnHCF in AZIBs, and explained it through the structural modification of the material, which we monitored with synchrotron-based x-ray techniques.

2. Experimental

2.1 Synthesis

The NiMnHCF was synthesized through a simple and scalable co-precipitation method[24,30]. The reagents manganese sulphate monohydrate ($MnSO_4 \cdot H_2O$), nickel sulphate ($NiSO_4$), sodium ferrocyanide decahydrate ($Na_4[Fe(CN)_6] \cdot 10H_2O$) and sodium sulphate ($Na_2SO_4$) were used without further purification (Sigma Aldrich). Aqueous solutions of $MnSO_4 \cdot H_2O$ and $NiSO_4$ were preliminary mixed in 90/10 ratio for 10% concentration of nickel. Afterwards, it was added dropwise, together with the aqueous solution of $Na_4[Fe(CN)_6] \cdot 10H_2O$, to an aqueous solution of Na_2SO_4 (0.1 L, of each 0.1000 M solution), by means of a peristaltic pump at a rate of 3.3 mL • min^{-1}, upon continuous stirring and constant temperature (40 ± 2 °C, regulating with a thermostatic bath). The obtained solution was aged for 5 days. After centrifugation, the solid fraction was washed three times with distilled water, dried at 60 °C for 48 h and grinded in an agate mortar. The formula of the synthesized material was obtained by means of microwave-plasma atomic emission spectroscopy (MP-AES), which was performed on MP-AES 4210 high sensitivity optical emission spectrometer, and thermogravimetric analysis (TGA), which was carried out in TA Discovery TGA instrument. Corresponding formula was: $Na_{1.4}Mn_{0.90}Ni_{0.10}[Fe(CN)_6]_{0.76} \cdot 3.4H_2O$.

2.2 Electrode Preparation

Dried samples were mixed with the carbon black as a conductive agent and polytetrafluoroethylene (PTFE) as a binder in a mortar. Active material, carbon black and PTFE ratio was 70:25:5. Afterwards, the pellets with 8 mm and 12 mm diameter were cut out, with the mass loading of approximately 8±1 $mg_{NiMnHCF} \cdot cm^{-2}$. Before the electrochemical tests sample soaking in the electrolyte solution under the vacuum was actively used, for at least 2 hours. Ni-containing MnHCF pellets were used as positive electrodes in the coin cells, 3 M $ZnSO_4$ aqueous solution as an electrolyte, Whatman paper as a separator, and Zn metal plate as the anode were implemented. Cyclic voltammetry was performed on CHI660 and CHI620 cyclic voltammeters, $1 < E < 1.9$ V versus Zn^{2+}/Zn, with scan rate of 0.2 mV • s^{-1}. For galvanostatic cycling Neware BTS4000-5V100mA Battery testing system was utilized, $1 < E < 1.85$ V versus Zn^{2+}/Zn, with current density of 20 mA • g^{-1}. Afterwards, charged and discharged state electrodes from various cycles have been extracted for the further *ex situ* analysis (**Table S1**).

2.3 X-ray Characterization Techniques

XAS experiments were conducted at Sincrotrone Elettra, Basovizza, Italy, at XAFS beamline, in transmission mode. K-edges of Mn, Fe, Ni and Zn were collected. The measurements were performed in the following ranges: 6344-7090 eV for Mn, 6917-8088 eV for Fe, 8155-8882 eV for Ni, and 9464-10637 eV for Zn. Before the edge, the measurement was performed in every 5 eV, near the edge region decreasing the interval to 0.2 eV, and increasing with constant k-dependence in EXAFS part. For Mn, Fe and Zn, up to k = 16 was recorded, and for Ni up to k = 12. Sample holder with 8 spaces was adopted, z coordinates were defined, and necessary horizontal and vertical gaps were set for optimal beam size for probing each sample[31]. XAS spectra were calibrated using the Athena software[32].

PXRD data were recorded at the MCX beamline at Sincrotrone Elettra, Basovizza, Italy[33,34]. The *operando* measurements were performed using the commercial El-cell[35], equipped with a beryllium window, where x-rays are able to penetrate. The material of interest was 12 mm diameter NiMnHCF cathode (mass loading 7.55 $mg_{NiMnHCF} \cdot cm^{-2}$). In this system Zn foil with a hole was used as an anode, Al-mesh as a current collector, and 3 M $ZnSO_4$ as an electrolyte. Galvanostatic cycling was performed between $1 < E < 1.85$ V versus Zn^{2+}/Zn, with a current density of 20 mA • g^{-1}. The analysis was performed at MCX beamline, with the x-ray beam

of 1.03318 Å, in reflection mode using the marCCD detector. Measurements were successful, even though this configuration for the battery-material research was a novelty on MCX beamline. The diffraction pattern was recorded with 20 second scans every 5 minutes, during the galvanostatic cycling of the El-cell.

For *ex situ* electrodes the monochromatic x-ray beams of 1.03318 Å and 0.62000 Å (for aged samples) were used, in the transmission mode with a marCCD detector. Samples were attached with paper-tape on sides, and in case of aged electrodes, they were embodied in double Kapton tape. The XRD pattern was collected with 0.01° steps and an acquisition time of 1 s/step. Background, Kapton tape and standard LaB_6 were also analyzed. The crystal structure was refined by GSAS II[36], and because of the different wavelength of x-ray beam for the *x*-axis of the diffractograms *Q* ($Å^{-1}$) was adopted, rather than 2θ (°).

3. Results and Discussion

3.1 Electrochemical Characterization

The full-cells were assembled with NiMnHCF as a cathode, metallic Zn sheet as an anode and 3 M $ZnSO_4$ as an electrolyte. During the initial charge, Na^+ is expected to leave the structure, and afterwards, upon the discharge process Zn^{2+} to enter, while in later cycles Zn^{2+} should reversibly intercalate in the hexacyanoferrate framework. As **Figure 1a** shows, during the CV tests, the voltammograms demonstrate initial several cycles to be different from the following ones, indicating to the activation process of the cathode material. Two oxidation peaks at around 1.6 V and 1.85 V from the first charging process can be attributed to the sodium extraction from the NiMnHCF framework, from low-spin Fe^{II}/Fe^{III} and high-spin Mn^{II}/Mn^{III}, respectively[37,38,39]. These signals are not only decreasing rapidly in the consecutive cycles, but the peak at the high potential splits into two at around 1.81 V and 1.86 V, respectively, and the wide peak at around 1.6 V shifts towards the low potential. Both can be explained by Zn extraction from the hexacyanoferrate framework, alongside the sodium. In the first discharge, corresponding reduction signals are observable: there is one wide peak, centered at 1.52 V, with weakly pronounced shoulder at 1.67 V. As their counterparts, the intensity decrease of the reduction peaks and the shift towards the higher potential occur. This instability suggests that the undergoing electrochemical reaction might be more complicated than expected.

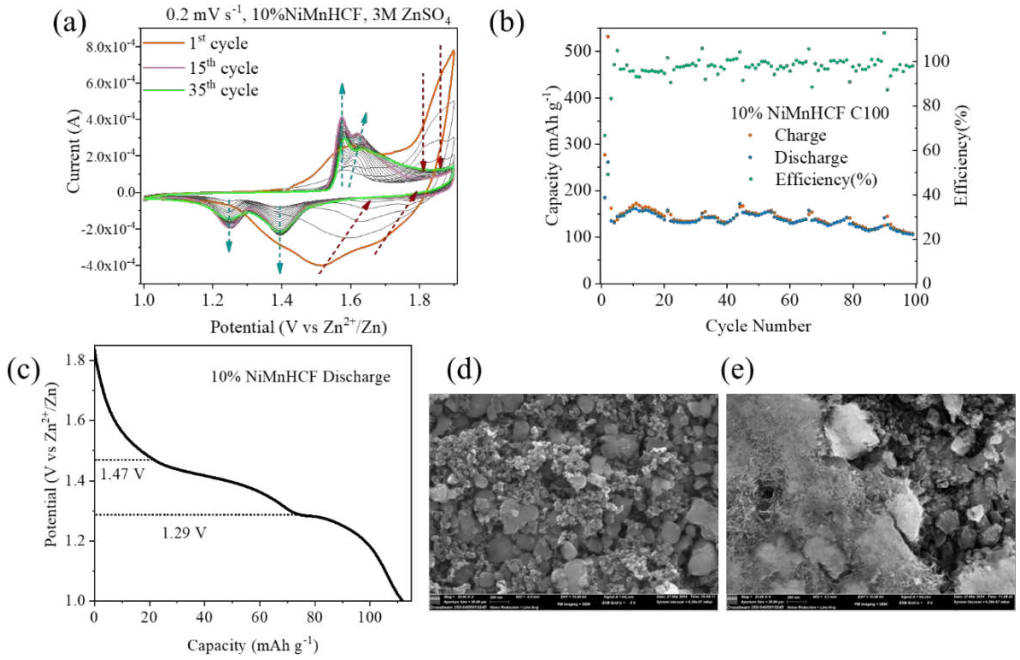

Figure 1. (a) the CV of Zn/NiMnHCF cell, scan rate 0.2 mV • s^{-1}, 1-1.9 V (V *vs*. Zn^{2+}/Zn); (b) the stability test during the galvanostatic cycling of Zn/NiMnHCF cell, current density 20 mA • g^{-1}, 1-1.85 V (V *vs*. Zn^{2+}/Zn); (c) corresponding discharge profile after the stabilization; (d) SEM image of Pristine sample of NiMnHCF at 25 kx magnification; (e) SEM image of C10 sample of NiMnHCF at 25 kx magnification

In the consecutive cycles new peaks are appearing, and slowly intensifying. The oxidation signals at 1.56 V and 1.6 V, and the reduction ones at 1.25 V and 1.4 V are replicating the Zn-ion battery behavior with MnO_2 cathode[40,41]. In this case, the two oxidation peaks might correspond to the Zn-extraction from the MnO_2 cathode as the Mn^{III}/Mn^{II} states undergo the oxidation to the Mn^{IV} state; and the reduction ones may represent Zn-insertion into the MnO_2, and cause the reduction of Mn^{IV} to the Mn^{III}/Mn^{II} states[41]. This hypothesis will be explored later in detail.

The galvanostatic charge/discharge of full-cell at a current density of 20 mA • g^{-1}, also showed the initial capacity-decrease during the activation stage, but after the stabilization, the battery retained over 100 mAh • g^{-1} capacity after 100 cycles (**Figure 1b**), which is improvement from the pure MnHCF with the similar system, reported before, where capacity reached only 70 mAh • g^{-1}, after 50 cycles on C/5 rate[38]. **Figure S1** shows the cycling performance of NiMnHCF at different current densities. The **Figure 1c** demonstrates the discharge curve during the galvanostatic cycling experiment (after the activation and stabilization, which needs approximately 5-10 cycles), and the plateaus are positioned at 1.29 V and 1.47 V, which is characteristic to the MnO_2 cathode material[41], rather than MnHCF or ZnHCF (in agreement with CV tests).

Additionally, the SEM images of Pristine and C10 *ex situ* sample showed the morphological alterations. As it is visible from **Figures 1d and S2**, the pristine electrode is homogeneous, there are some small particles (carbon) and larger aggregates (active material) observable; however, in **Figures 1e and S3** morphological modifications are evident: the fibrous structure can be related to the separator, but there are other larger aggregates. Also, according to 2D-XRF images, the original homogeneous metal distribution in pristine electrode has modified in C10 (**Figure S4**). These alterations are additional indication of the structural modification, which is later explored in details with advanced x-ray techniques.

3.2 XAS Measurement

As mentioned above, the dissolution of Mn and its substitution with Zn is a serious issue for the MnHCF cathode material, and the presence of Ni ions, apparently was not able to hinder this process in AZIBs. The formation of MnO_2 phase, suggested from the electrochemical tests, can be only explained by the dissolution of Mn from the hexacyanoferrate framework. To explore this hypothesis, *ex situ* XAS experiment has been conducted. Generally, in MnHCF both Mn and Fe sites are active, while in NiHCF, only Fe[28,29]. These three metals, alongside with Zn have been investigated. During the cycling process Fe was not dramatically affected: edge jump position in-between charged and discharged states remained the same (**Figure S5**). The only difference concerned the pre-edge region. The electronic transitions of LS Fe are $1s \rightarrow t_{2g}$ and $1s \rightarrow e_g$, corresponding to the pre-edge peaks at ≈ 7111.2 eV and ≈ 7114.2 eV, respectively[42]. However, $1s \rightarrow t_{2g}$ transition, which can only occur in Fe^{III}, in this experiment was only visible in the C1 sample (**Figure 2a**), indicating to the low amount of overall oxidized Fe content in the charged electrodes of the later cycles. This is in a good agreement with electrochemical tests, where hexacyanoferrate contribution was also slowly disappearing.

The Fourier transform of Fe K-edge spectra on **Figure 2b** shows three coordination shells. According to the hexacyanoferrate framework, the first peak was assigned to carbon (Fe-C), the second to nitrogen (Fe-C-N), and the third to manganese (Fe-C-N-Mn) or nickel (Fe-C-N-Ni)[24]. During the cycling, only the last peak shape was modified, which might be the indication to the Mn-Zn replacement during the insertion/extraction of Zn-ions. Same was observed on zinc K-edge spectra on **Figure 2c**, as it replicated the Zn spectrum of ZnHCF material[38]. It appears that Zn started occupying the position of Mn in hexacyanoferrate framework from the first cycle, with increasing edge jump intensity upon the cycling, indicating that higher portions of manganese were getting substituted.

Even though nickel was not suspected of any electrochemical activity, for the exploration of its neighbourhood, the K-edge of Ni was also recorded. Indeed, no alteration of the spectrum shape was detected during the cycling process, however, the dramatical decrease of signal intensity indicated that dissolution had affected not only Mn, but Ni as well (**Figure 2d**).

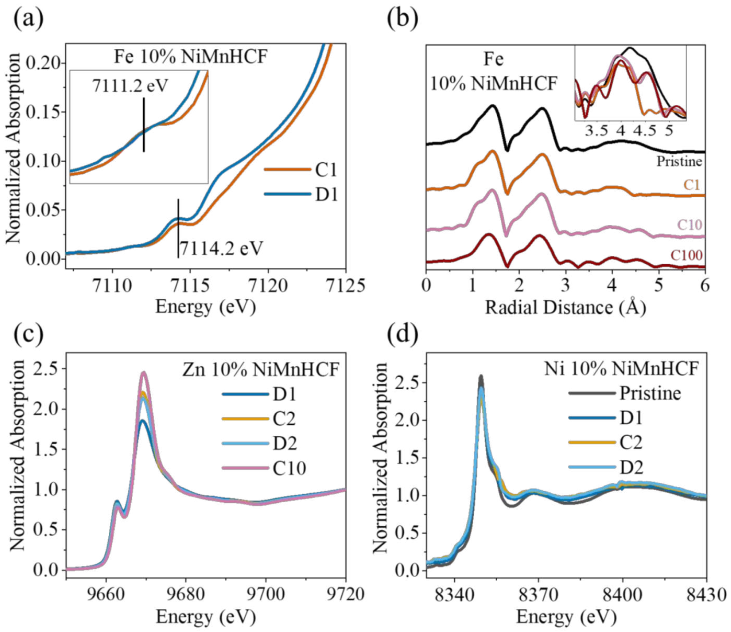

Figure 2. XAS measurement results of NiMnHCF *ex situ* electrodes: (a) Pre-edge region of Fe K-edge; (b) Fourier transform of Fe K-edge; (c) Zn K-edge; (d) Ni K-edge

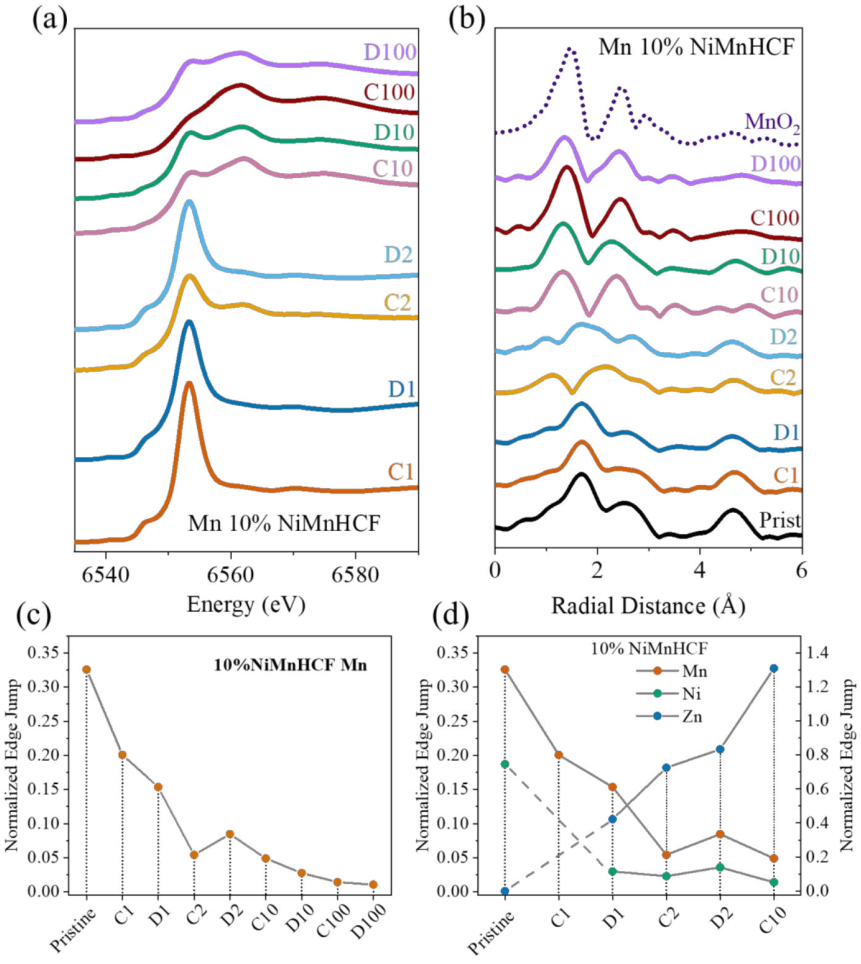

Figure 3. XAS measurement results of NiMnHCF *ex situ* electrodes: (a) Mn K-edge; (b) Fourier transform of Mn K-edge, together with MnO_2 standard; (c) Mn edge jump intensity dynamics; (d) Mn, Ni and Zn edge jump intensity dynamics

The most crucial part of XAS analysis definitely concerns Mn. As **Figure 3a** shows, the modifications of the spectra indicated the changes in both, the oxidation state and the local structure. Even the first cycle differed from the pristine electrode, and with further cycles the alteration deepened. For the initial cycles the most evident change was the peak intensity decrease, however by the 10th cycle the shape of the entire spectra had been modified so drastically, that it clearly represented different Mn species from the hexacyanoferrate framework. From the 10th to the 100th cycle no major modifications were observed, which indicated the stability of the new structure on the local scale. The edge jump intensity decrease, indicating to the Mn dissolution, was more rapid with the initial cycles (**Figure 3c**). This trend is in agreement with the reduction of Ni and the increase of Zn edge jumps (**Figure 3d**). Local structure alteration is especially easy to observe in the Fourier transform spectra (**Figure 3b**): the modification of the first and the second shell of Mn were undoubtfully present. The reference MnO_2 Fourier transform spectrum is very similar to the ones of cycled sample – the position and the intensity ratio of the first and the second coordination shell match.

The Mn Fourier transform spectra results agree with the ones for Fe, as they also indicated the changes in the third coordination shell, which initially was Mn (together with Ni). The spectra of C2/D2 samples showed the intermediate pattern between the 1st and the 10th cycle.

For the better understanding of what exactly happened to Mn inside the structure, linear combination fitting (LCF) was performed on the Mn K-edge spectra of the cycled electrodes. As standards pristine, $MnSO_4$ and several manganese oxides (MnO, Mn_3O_4, Mn_2O_3 and MnO_2) were used. From **Figure 4**, it is clearly visible, that a definitive outcome was not possible to achieve. But the results still can be used as a strong indicator, that there was a mixed distribution of the manganese species inside the pellets. The contribution of Mn in hexacyanoferrate structure was non-uniformly decreasing with aging, and in the 10th cycle only around 5% of the Mn appeared to be in this position. On the other hand, MnO_2 was contributing an increasing part of the fit, the charged samples quite logically having higher amounts of Mn^{4+} than the corresponding discharged samples of the same cycle; according to LCF, from the remaining Mn, MnO_2 form in C1 was just below 20%, increasing to above 42% in C2, to 65% in C10 and more than 80% in C100 (as mentioned, less in the corresponding discharged samples) (**Table 1**).

Table 1. The LCF results of Mn K-edge in different charge states of NiMnHCF cathode material

	Sample	**Pristine**	**$MnSO_4$**	**MnO**	**Mn_3O_4**	**Mn_2O_3**	**MnO_2**	**R-factor**	**Reduced χ^2**
Ratio	C1	0.391	0.144	0.272	0	0	0.194	0.00671	0.00350
(Error)		(0.008)	(0.103)	(0.037)	(0.062)	(0.065)	(0.034)		
Ratio	D1	0.277	0.322	0.269	0	0	0.132	0.00581	0.00250
(Error)		(0.006)	(0.087)	(0.031)	(0.052)	(0.055)	(0.029)		
Ratio	C2	0.140	0.224	0.211	0	0	0.424	0.00486	0.00137
(Error)		(0.005)	(0.065)	(0.023)	(0.039)	(0.041)	(0.021)		
Ratio	D2	0.254	0.201	0.289	0	0	0.256	0.00739	0.00282
(Error)		(0.007)	(0.093)	(0.033)	(0.055)	(0.058)	(0.031)		
Ratio	C10	0.044	0.132	0.140	0.035	0	0.650	0.00568	0.00138
(Error)		(0.005)	(0.064)	(0.023)	(0.039)	(0.041)	(0.021)		
Ratio	D10	0.056	0.167	0.143	0	0	0.635	0.00424	0.00103
(Error)		(0.004)	(0.056)	(0.020)	(0.033)	(0.035)	(0.019)		
Ratio	C100	0.001	0.149	0	0	0.042	0.808	0.01173	0.00276
(Error)		(0.006)	(0.088)	(0.029)	(0.051)	(0.052)	(0.028)		
Ratio	D100	0.042	0.185	0.093	0	0	0.680	0.01106	0.00261
(Error)		(0.006)	(0.086)	(0.028)	(0.049)	(0.050)	(0.027)		

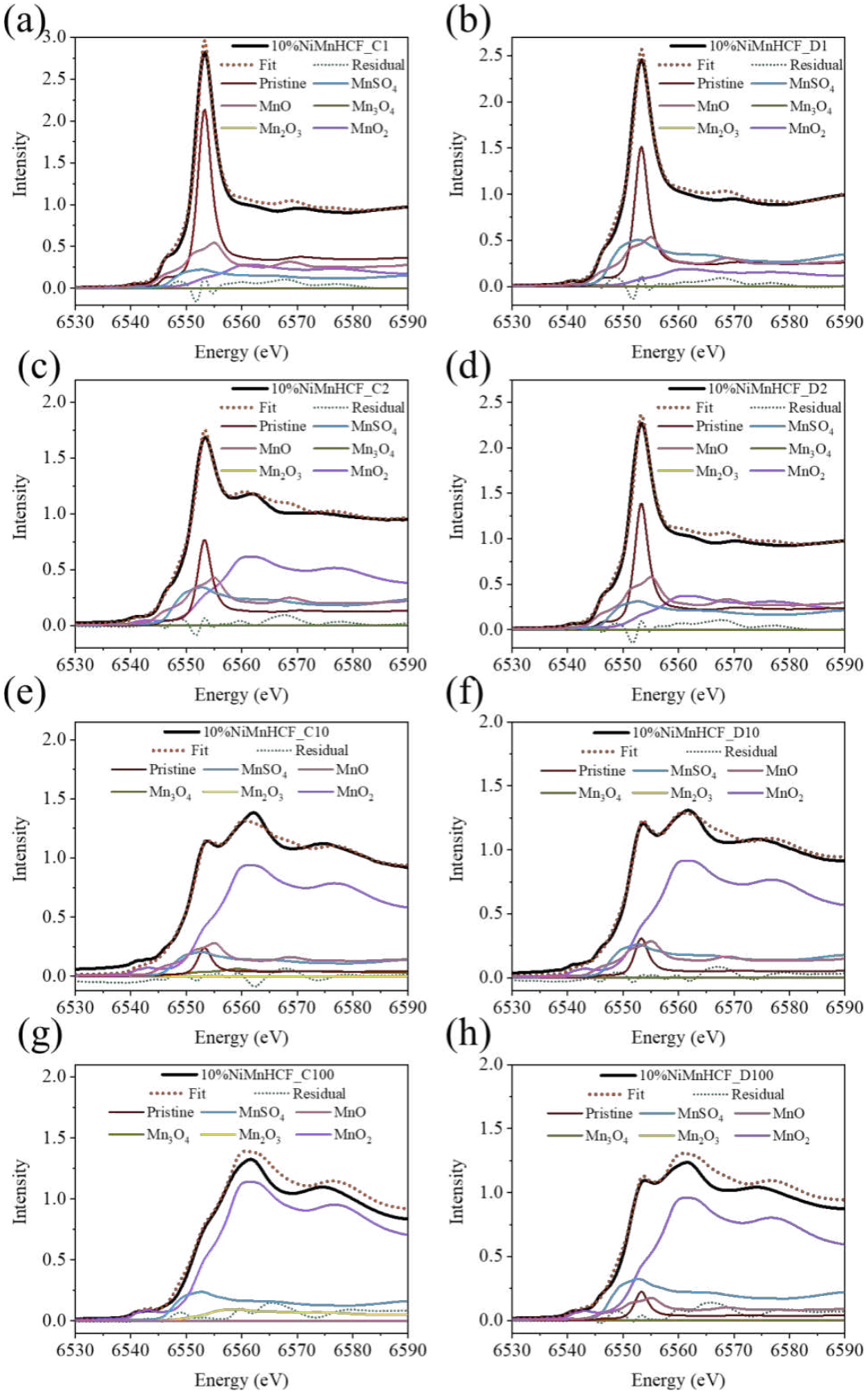

Figure 4. The LCF of Mn K-edge of NiMnHCF: (a) C1; (b) D1; (c) C2; (d) D2; (e) C10; (f) D10; (g) C100 and (h) D100

3.3 *Operando* PXRD Measurements

The structure of NiMnHCF cathodes was also checked with synchrotron based PXRD technique. The powder samples had face centred cubic symmetry, F m-3m space group, a = 10.4837 Å, as reported before[30]. Pristine electrode kept F m-3m symmetry, with the slight decrease of the cell volume: a = 10.43 Å.

The *operando* measurement of NiMnHCF cathode material was performed with the commercial El-cell, in the reflection mode. Diffractograms were recorded during the galvanostatic cycling of the battery. **Figures 5a and S6** show the stack of the obtained diffractograms. Visible changes occurred inside the structure: the new peaks emerged during the charging process at the higher angles from the original reflections: at 1.19 $Å^{-1}$, 1.69 $Å^{-1}$, 2.39 $Å^{-1}$, from which during the discharge process the first reflection decreased partially, the second disappeared completely, and the third one remained unchanged. Also, during the charging process, a shoulder appeared at 2.68 $Å^{-1}$ (the reflection on 2.66 $Å^{-1}$, belongs to Al from the current collector), alongside the smaller peaks (depicted with green arrows), which remained during the consecutive discharge process. Therefore, the structure appears to be only partially reversible during the initial charge-discharge process.

One of the main advantages of the *operando* measurement is the possibility to observe the dynamics of the system. The PXRD patterns extracted at different voltages demonstrated that the main modifications started only after the plateau at ≈1.77 V, and afterwards the intensities of the new reflections slowly rose with increasing voltage. Similarly, during the discharge, the alterations start occurring from the plateau below ≈1.63 V, and became more rapid at a lower voltage (**Figures 5b, 5c, S7 and S8**).

Even though the *operando* measurements have a huge advantage in means of understanding the processes happening inside the system in real time, low resolution makes it difficult to perform the exact phase identification. Therefore, *ex situ* measurements were also conducted alongside the *operando* test.

3.4 *Ex situ* PXRD Measurements

The results of *ex situ* PXRD were aligned with the *operando* measurement. Indeed, the structural modifications started from the first charging process, also in agreement with XAS analysis. Alongside the modification of the cell parameters and strain inside the system, the emergence of a new phase was also detected. All diffractograms are stacked on **Figure 5d.** The C1 sample can be characterized as a sum of two phases, the original F m-3m, and a new primitive cubic cell P m-3m with larger a parameter (a = 11.93 Å). These modifications seem to have been not reversible, as the D1 structure did not resemble pristine electrode, and was still a mixture of two phases. With further cycling the transformation continued, and the original phase kept slowly disappearing. The initial F m-3m phase was not visible in the tenth cycle of either charge state. As **Figure 5d** shows, the structure of C10 and D10 were almost identical, and highly crystalline. The Pawley refinement of the 10^{th} cycle was performed with P m-3m phase reaching low R_{wp}=2.377 (**Figure S9**), however the fit became better (R_{wp} = 1.696), especially in high Q values, after the refinement with two phases: P m-3m, together with the hexagonal R -3c (**Figure S10**), which has widely been reported as a common ZnHCF phase[43]. Therefore, we can attribute P m-3m to be an intermediate step between the face centered cubic NiMnHCF structure, as it modifies through Ni and Mn dissolution into the hexagonal ZnHCF. This phenomenon could be connected to the initial activation cycles in the battery system, before the stabilization.

The 100^{th} cycle of NiMnHCF again displayed the presence of multiple phases inside the structure, however the initial refinement, performed on two phases (P m-3m and R -3c) was improved after adding the third phase, coming from the electrolyte, the monoclinic P 21/c unit cell, characteristic to the hydrated zinc sulphate ($ZnSO_4 \cdot 4H_2O$) (**Figures S11 and S12**).

Therefore, MnO_2 was not detected in PXRD measurement at all, which at first might seem suspicious, but in the literature, there are reports about the high performance amorphous MnO_2 as a cathode material. Indeed, both electrochemical tests showed highly similar results to the work done by Huang *et al.*[41]. The absence of the MnO_2 in diffractograms can be explained by the lack of crystallinity, which is a necessary requirement for the PXRD measurement. On the other hand, it was possible to witness with XAS, where short range order is enough for the detection of the material.

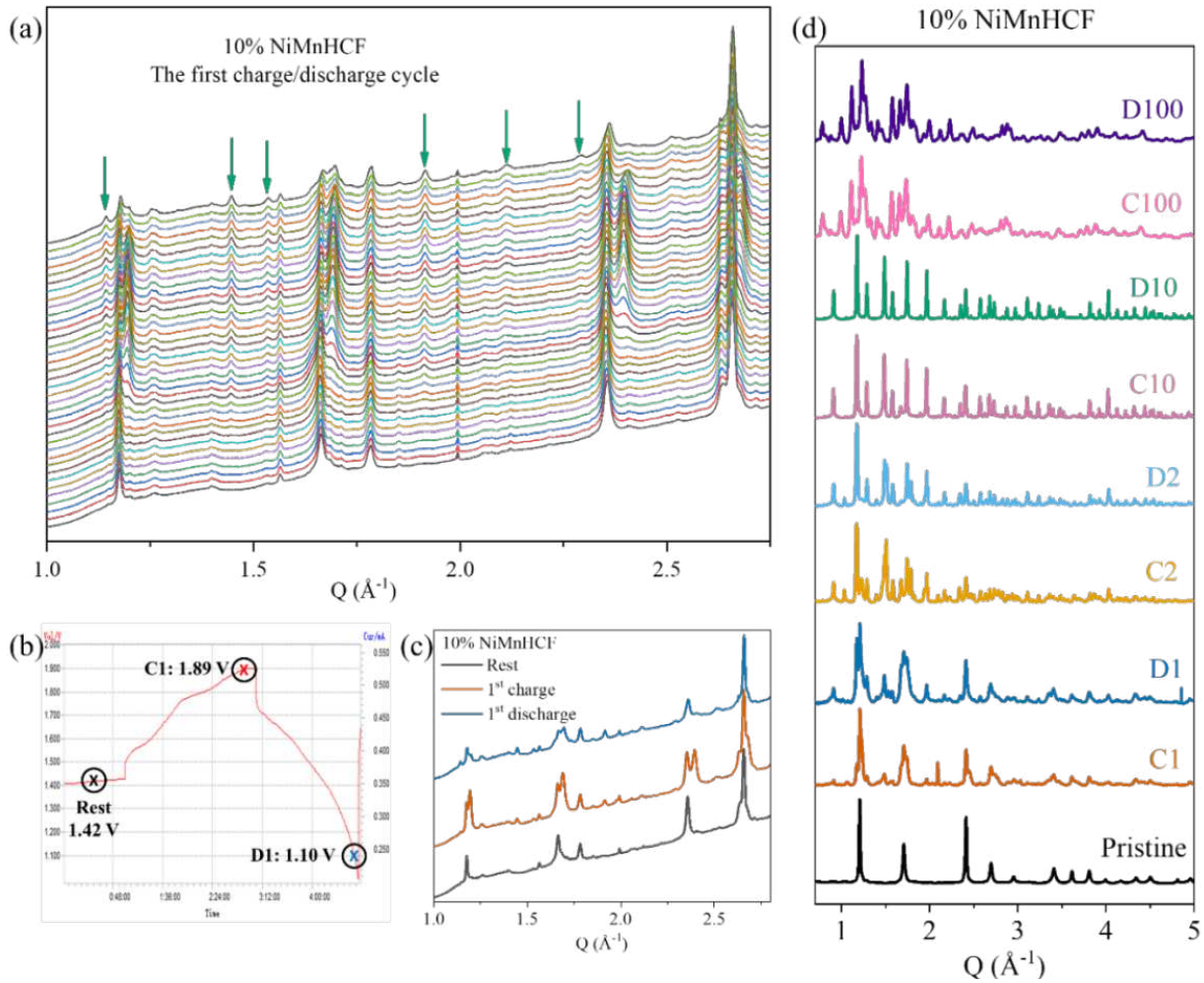

Figure 5. PXRD measurement results of NiMnHCF (a) in *operando* modality the first cycle of Zn/NiMnHCF cell, current density 20 mA•g^{-1}, 1-1.85 V (V *vs*. Zn^{2+}/Zn); (b) corresponding charge/discharge profile, with three points chosen as Rest (OCP), C1 and D1; (c) the diffractograms recorded at Rest, C1 and D1 points; (d) diffractograms of *ex situ* electrodes: pristine, C1, D1, C2, D2, C10, D10, C100 and D100 (from down to up)

4. Conclusions

Both electrochemical tests and advanced synchrotron-based x-ray characterization techniques demonstrated the strong modification inside the NiMnHCF cathode material. The initial capacity decay was connected to the structural alteration, which was further stabilized by the formation of MnO_2 and ZnHCF phases, with the former one contributing most of the electrochemical activity, proved by CV, galvanostatic cycling and XAS measurement. XAS technique also demonstrated the penetration of Zn inside the hexacyanoferrate framework, and the alteration of Mn species, mostly towards the formation of MnO_2.

The *operando* PXRD measurement provided the possibility to analyse the cathode during the operational conditions, which was extremely important for understanding the dynamics of the system, and being able to follow the gradual structural modifications inside the electrode. While, *ex situ* measurements proved the modification of the material through the phase transformation from the face centered cubic unit cell to primitive cubic to hexagonal, with the additional electrolyte contribution. The diffraction patterns did not prove the existence of MnO_2, which can be explained by the amorphous nature of the newly formed oxide.

Together, electrochemical characterization and advanced x-ray techniques were able to shed a light to the electrochemical behavior of the NiMnHCF cathode material in AZIBs. The modification of the initial phase indicates that Ni not only failed to stabilize

MnHCF cathode in AZIB system, but was affected by the dissolution itself. However, the new mixed phase appeared to be stable, and provide capacity over 100 mAh • g^{-1} over 100 cycles.

Acknowledgements

Measurements at Elettra were supported by project #20212162 and #20222183 (M.G. as PI). M.M. acknowledges the CERIC-ERIC consortium for providing the PhD scholarship. The work was also supported by the RFO funds of the University of Bologna. MUR is acknowledged for the partial support through the Sustainable Mobility Center, Centro Nazionale per la Mobilita′ Sostenibile-CNMS, Spoke 6 (NEST) of the National Recovery and Resilience Plan (NRRP).

Author's Contributions

Investigation: Maisuradze M, Li M, Gaboardi M, Aquilanti G, Plaisier JR

Data curation: Maisuradze M, Li M, Gaboardi M, Aquilanti G, Plaisier JR and Giorgetti M

Formal analysis, visualization, writing-original draft: Maisuradze M

Writing-review & editing: Maisuradze M, Li M and Giorgetti M

Conceptualization, supervision, methodology: Giorgetti M

Availability of Supporting Data

Supporting information at the end of the article.

Conflict of Interest

The authors declare no conflict of interest.

References

[1] Contemporary Amperex Technology Co., Ltd. Ningde, Fujian, China. CATL Unveils Its Latest Breakthrough Technology by Releasing Its First Generation of Sodium-ion Batteries. Available from: https://www.catl.com/en/news/665.html [Last accessed on 20 November 2023]

[2] Fang G, Zhou J, Pan A, *et al*. Recent advances in aqueous zinc-ion batteries. *ACS Energy Letters*, 2018;3(10):2480-2501. https://doi.org/10.1021/acsenergylett.8b01426

[3] Konarov A, Voronina N, Jo JH, *et al*. Present and future perspective on electrode materials for rechargeable zinc-ion batteries. *ACS Energy Letters*, 2018;3(10):2620-2640. https://doi.org/10.1021/acsenergylett.8b01552

[4] Grignon E, Battaglia AM, Schon TB, *et al*. Aqueous zinc batteries: design principles toward organic cathodes for grid applications. *IScience*, 2022;25(5):104204. https://doi.org/10.1016/j.isci.2022.104204

[5] Qian J, Wu C, Cao Y, *et al*. Prussian blue cathode materials for sodium-ion batteries and other ion batteries. *Advanced Energy Materials*, 2018;8(17):1702619. https://doi.org/10.1002/aenm.201702619

[6] Shibata T and Moritomo Y. Ultrafast cation intercalation in nanoporous nickel hexacyanoferrate. *Chemical Communications*, 2014;50(85):12941-12943. https://doi.org/10.1039/C4CC04564E

[7] Takachi M, Fukuzumi Y and Moritomo Y. Na^+ diffusion kinetics in nanoporous metal-hexacyanoferrates. *Dalton Transactions*, 2016;45(2):458-461. https://doi.org/10.1039/C5DT03276H

[8] You Y, Wu XL, Yin YX, *et al*. A zero-strain insertion cathode material of nickel ferricyanide for sodium-ion batteries. *Journal of Materials Chemistry A*, 2013;1(45):14061-14065. https://doi.org/10.1039/c3ta13223d

[9] Wessells CD, Peddada SV, Huggins RA, *et al*. Nickel hexacyanoferrate nanoparticle electrodes for aqueous sodium and potassium ion batteries. *Nano Letters*, 2011;11(12):5421-5425. https://doi.org/10.1021/nl203193q

[10] Imanishi N, Morikawa T, Kondo J, *et al*. Lithium intercalation behavior into iron cyanide complex as positive electrode of lithium secondary battery. *Journal of Power Sources*, 1999;79(2):215-219. https://doi.org/10.1016/S0378-7753(99)00061-0

[11] Eftekhari A. Potassium secondary cell based on Prussian blue cathode. *Journal of Power Sources*, 2004;126(1-2):221-228.

https://doi.org/10.1016/j.jpowsour.2003.08.007

[12] Wessells CD, Huggins RA and Cui Y. Copper hexacyanoferrate battery electrodes with long cycle life and high power. *Nature Communications*, 2011;2(1):550. https://doi.org/10.1038/ncomms1563

[13] Wang RY, Shyam B, Stone KH, *et al*. Reversible multivalent (monovalent, divalent, trivalent) ion insertion in open framework materials. *Advanced Energy Materials*, 2015;5(12):1401869. https://doi.org/10.1002/aenm.201401869

[14] Mizuno Y, Okubo M, Hosono E, *et al*. Electrochemical Mg^{2+} intercalation into a bimetallic CuFe Prussian blue analog in aqueous electrolytes. *Journal of Materials Chemistry A*, 2013;1(42):13055-13059. https://doi.org/10.1039/c3ta13205f

[15] Park H, Lee Y, Ko W, *et al*. Review on cathode materials for sodium-and potassium-ion batteries: structural design with electrochemical properties. *Batteries & Supercaps*, 2023;6(3):e202200486. https://doi.org/10.1002/batt.202200486

[16] Li M, Bina A, Maisuradze M, *et al*. Symmetric aqueous batteries of titanium hexacyanoferrate in Na^+, K^+, and Mg^{2+} media. *Batteries*, 2021;8(1):1. https://doi.org/10.3390/batteries8010001

[17] Li M, Maisuradze M, Sciacca R, *et al*. A structural perspective on Prussian blue analogues for aqueous zinc-ion batteries. *Batteries & Supercaps*, 2023;6(11):e202300340. https://doi.org/10.1002/batt.202300340

[18] Jia Z, Wang B and Wang Y. Copper hexacyanoferrate with a well-defined open framework as a positive electrode for aqueous zinc ion batteries. *Materials Chemistry and Physics*, 2015;149:601-606. https://doi.org/10.1016/j.matchemphys.2014.11.014

[19] Li M, Gaboardi M, Mullaliu A, *et al*. Influence of vacancies in manganese hexacyanoferrate cathode for organic Na-ion batteries: a structural perspective. *ChemSusChem*, 2023; 16(12):e202300201. https://doi.org/10.1002/cssc.202300201

[20] Cao T, Zhang F, Chen M, *et al*. Cubic manganese potassium hexacyanoferrate regulated by controlling of the water and defects as a high-capacity and stable cathode material for rechargeable aqueous zinc-ion batteries. *ACS Applied Materials & Interfaces*, 2021;13(23):26924-26935. https://doi.org/10.1021/acsami.1c04129

[21] Deng W, Li Z, Ye Y, *et al*. Zn^{2+} induced phase transformation of $K_2MnFe(CN)_6$ boosts highly stable zinc-ion storage. *Advanced Energy Materials*, 2021;11(31):2003639. https://doi.org/10.1002/aenm.202003639

[22] Ni G, Hao Z, Zou G, *et al*. Potassium manganese hexacyanoferrate with improved lifespan in $Zn(CF_3SO_3)_2$ electrolyte for aqueous zinc-ion batteries. *Sustainable Energy & Fuels*, 2022;6(5):1353-1361. https://doi.org/10.1039/D1SE02003J

[23] Lu Y, Wang L, Cheng J, *et al*. Prussian blue: a new framework of electrode materials for sodium batteries. *Chemical Communications*, 2012;48(52):6544. https://doi.org/10.1039/c2cc31777j

[24] Mullaliu A, Asenbauer J, Aquilanti G, *et al*. Highlighting the reversible manganese electroactivity in Na-rich manganese hexacyanoferrate material for Li- and Na-ion storage. *Small Methods*, 2019;4(1):1900529. https://doi.org/10.1002/smtd.201900529

[25] Gao C, Lei Y, Wei Y, *et al*. Coexistence of two coordinated states contributing to high-voltage and long-life Prussian blue cathode for potassium ion battery. *Chemical Engineering Journal*, 2022;431(1):133926. https://doi.org/10.1016/j.cej.2021.133926

[26] Zhou J, Wang Y Wang Z, *et al*. Co/Mn ratio-regulated hexacyanoferrates as a long-life and high-rate cathode for aqueous Zn-ion batteries. *Journal of Alloys and Compounds*, 2024;976:173158. https://doi.org/10.1016/j.jallcom.2023.173158

[27] Fu H, Liu C, Zhang C, *et al*. Enhanced storage of sodium ions in Prussian blue cathode material through nickel doping. *Journal of Material Chemistry A*, 2017;5(20):9604-9610. https://doi.org/10.1039/C7TA00132K

[28] Hu P, Peng W. Wang B, *et al*. Concentration-gradient Prussian blue cathodes for Na-ion

batteries. *ACS Energy Letters*, 2020;5(1):100-108. https://doi.org/10.1021/acsenergylett.9b02410

[29] Yang D, Xu J, Liao XZ, *et al*., Structure optimization of Prussian blue analogue cathode materials for advanced sodium ion batteries. *Chemical Communications*, 2014;50(87):13377-13380. https://doi.org/10.1039/C4CC05830E

[30] Maisuradze M, Li M, Aquilanti G, *et al*. Characterization of partially Ni substituted manganese hexacyanoferrate cathode material. *Materials Letters*, 2023;330:133259. https://doi.org/10.1016/j.matlet.2022.133259

[31] Cicco A Di, Aquilanti G, Minicucci M, *et al*. Novel XAFS capabilities at ELETTRA synchrotron light source. *Journal of Physics: Conference Series*, 2009;190:012043. https://doi.org/10.1088/1742-6596/190/1/012043

[32] Ravel B and Newville M. ATHENA, ARTEMIS, HEPHAESTUS: data analysis for X-ray absorption spectroscopy using IFEFFIT. *Journal of Synchrotron Radiation*, 2005;12(4):537-541. https://doi.org/10.1107/S0909049505012719

[33] Rebuffi L, Plaisier JR, Abdellatief M, *et al*. MCX: a synchrotron radiation beamline for X-ray diffraction line profile analysis. *Zeitschrift für Anorganische und Allgemeine Chemie*, 2014;640(15):3100-3106. https://doi.org/10.1002/zaac.201400163

[34] Plaisier JR, Nodari L, Gigli L, *et al*. The X-ray diffraction beamline MCX at Elettra: a case study of non-destructive analysis on stained glass. *ACTA IMEKO*, 2017;6(3):71. https://doi.org/10.21014/acta_imeko.v6i3.464

[35] EL-CELL GmbH. ECC-Opto-Std-Aqu. Test cell for optical characterization in the reflective mode with face-to-face arrangement of electrodes. For aqueous electrochemistry. Accessed January 24, 2024. https://www.el-cell.com/products/test-cells/optical-test-cells/ecc-opto-std-aqu/#1489741620679-37ccaee8-12f2

[36] Toby BH and Von Dreele RB. GSAS-II: the genesis of a modern open-source all purpose crystallography software package. *Journal of Applied Crystallography*, 2013;46(2):544-549. https://doi.org/10.1107/S0021889813003531

[37] Hou Z, Zhang X, Li X, *et al*. Surfactant widens the electrochemical window of an aqueous electrolyte for better rechargeable aqueous sodium/zinc battery. *Journal of Materials Chemistry A Mater*. 2017;5(2):730-738. https://doi.org/10.1039/C6TA08736A

[38] Li M, Sciacca R, Maisuradze M, *et al*. Electrochemical performance of manganese hexacyanoferrate cathode material in aqueous Zn-ion battery. *Electrochimica Acta*, 2021;400:139414. https://doi.org/10.1016/j.electacta.2021.139414

[39] Oliver-Tolentino MA, Vázquez-Samperio J, Arellano-Ahumada SN, *et al*. Enhancement of stability by positive disruptive effect on Mn-Fe charge transfer in vacancy-free Mn-Co hexacyanoferrate through a charge/discharge process in aqueous Na-ion batteries. *The Journal of Physical Chemistry* C, 2018;122(36):20602-20610. https://doi.org/10.1021/acs.jpcc.8b05506

[40] Huang C, Wu C, Zhang Z, *et al*. Crystalline and amorphous MnO_2 cathodes with open framework enable high-performance aqueous zinc-ion batteries. *Frontiers of Materials Science*, 2021;15(2):202-215. https://doi.org/10.1007/s11706-021-0551-y

[41] Alfaruqi MH, Mathew V, Gim J, *et al*. Electrochemically induced structural transformation in a γ-MnO_2 cathode of a high capacity zinc-ion battery system. *Chemistry of Materials*, 2015;27(10):3609-3620. https://doi.org/10.1021/cm504717p

[42] Mullaliu A, Conti P, Aquilanti G, *et al*. *operando* XAFS and XRD study of a Prussian blue analogue cathode material: iron hexacyanocobaltate. *Condensed Matter*, 2018;3(4):36. https://doi.org/10.3390/condmat3040036

[43] Rodríguez-Hernández J, Reguera E, Lima E, *et al*. An atypical coordination in hexacyanometallates: structure and properties of hexagonal zinc phases. *Journal of Physics and Chemistry of Solids*, 2007;68(9):1630-1642. https://doi.org/10.1016/j.jpcs.2007.03.054

Supplementary Information

Table S1. The list of the *ex situ* samples of NiMnHCF cathode material

NiMnHCF Samples	Description
Pristine	Fresh electrode
C1	Charged after 1st cycle
D1	Discharged after 1st cycle
C2	Charged after 2nd cycle
D2	Discharged after 2nd cycle
C10	Charged after 10th cycle
D10	Discharged after 10th cycle
C100	Charged after 100th cycle
D100	Discharged after 100th cycle

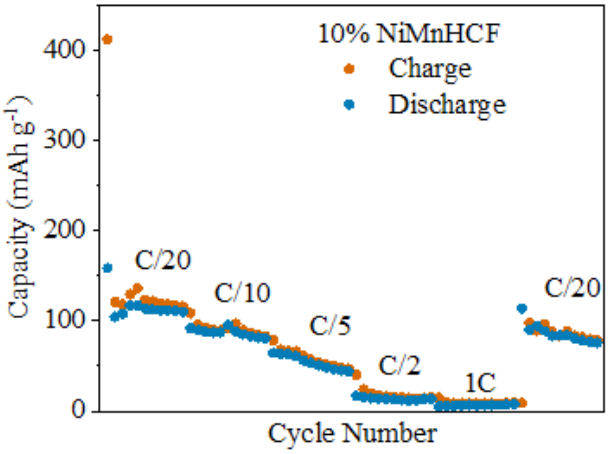

Figure S1. Cycling performance of NiMnHCF at different current densities

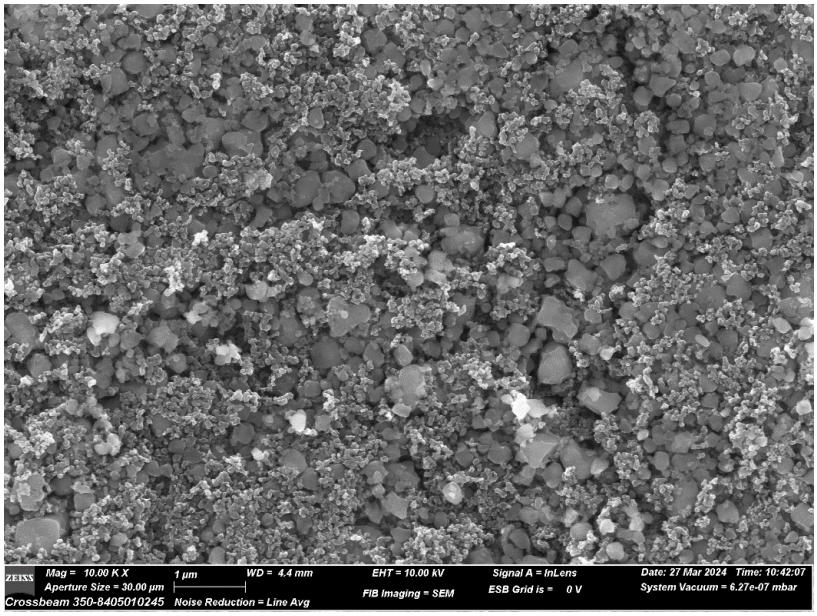

Figure S2. SEM image of Pristine sample of NiMnHCF at 10 kx magnification

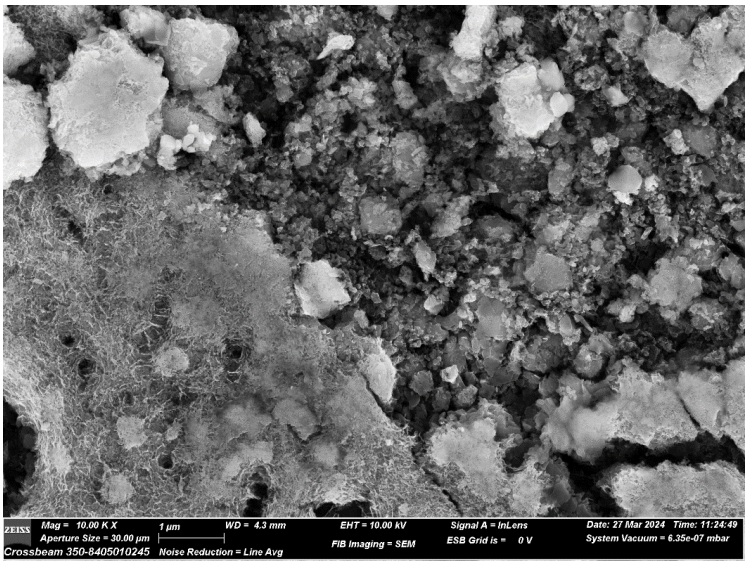

Figure S3. SEM image of C10 sample of NiMnHCF at 10 kx magnification

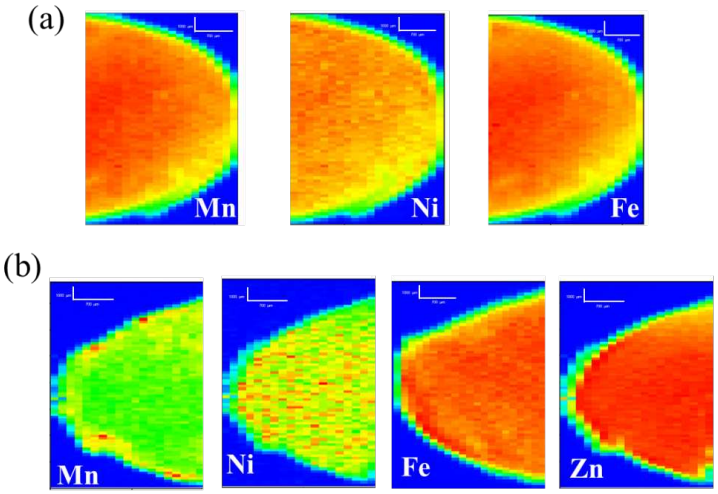

Figure S4. Normalized 2D-XRF maps of NiMnHCF *ex situ* electrode: (a) Pristine: Mn, Ni, Fe; (b) C10: Mn, Ni, Fe, Zn; intensity scale is color-based (red = high intensity; blue = low intensity); Length scale-vertical bar 1000 µm (200 µm x 5 px), horizontal bar 700 µm (140 µm x 5 px)

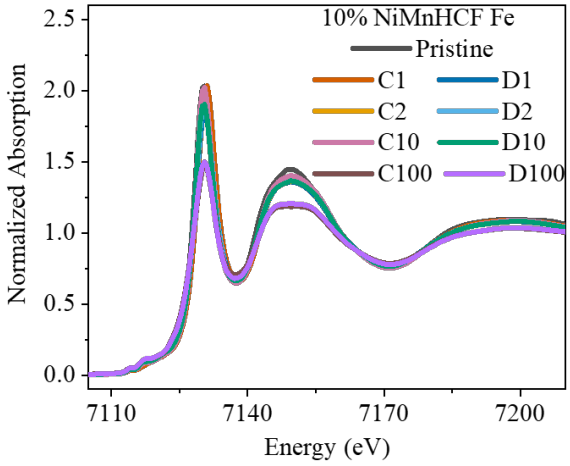

Figure S5. XAS measurement results of Fe K-edge of NiMnHCF *ex situ* electrodes

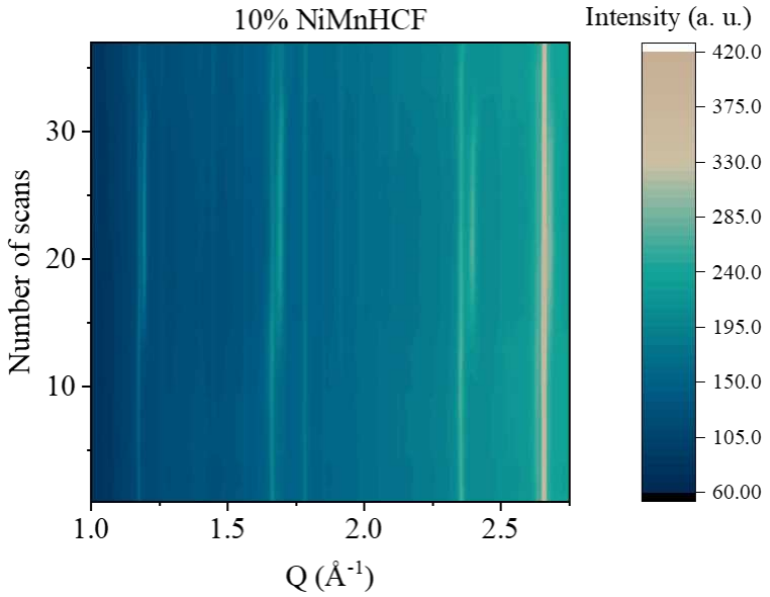

Figure S6. The contour plot of *operando* PXRD measurement results of the first cycle of Zn/NiMnHCF cell, 20 mA•g^{-1}, 1-1.85 V (V *vs*. Zn^{2+}/Zn)

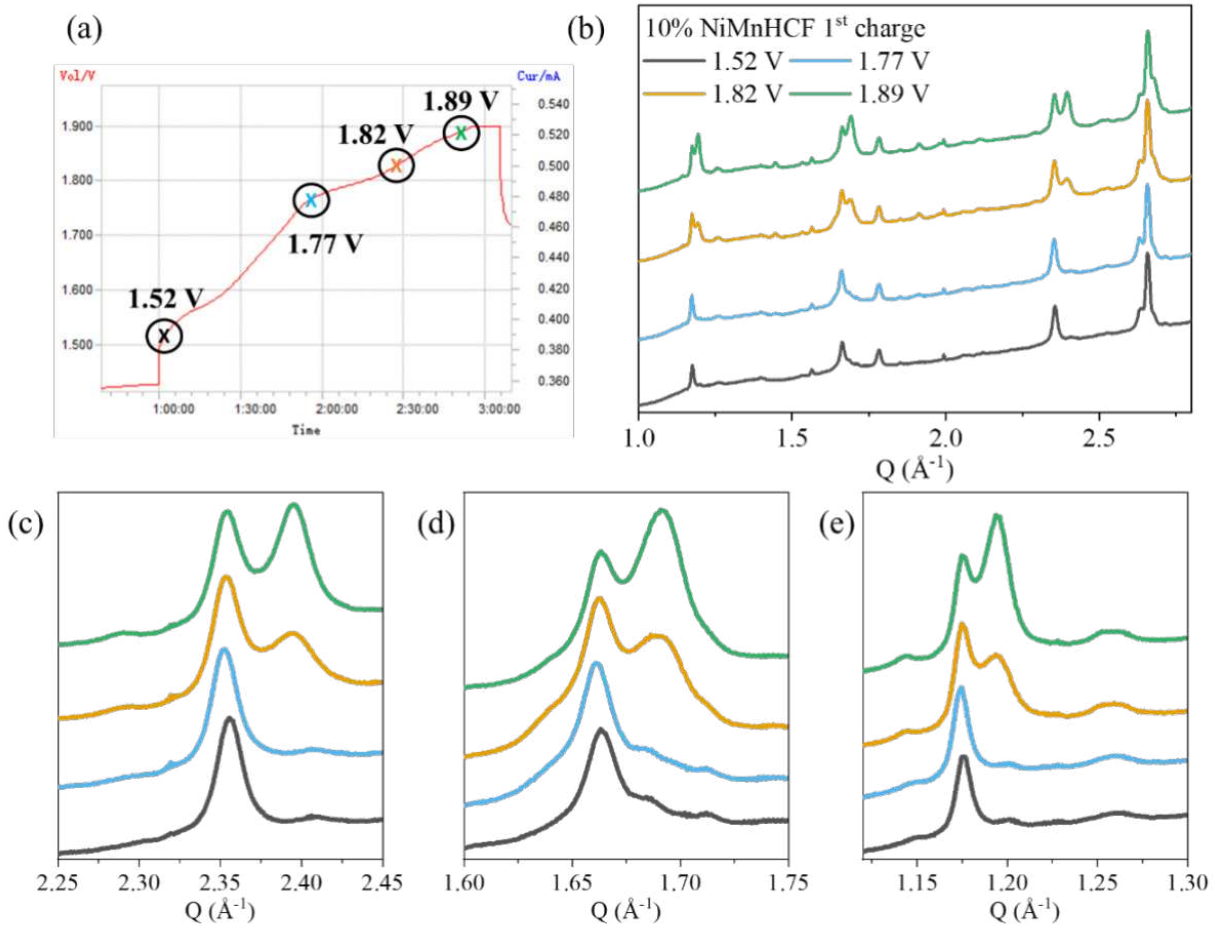

Figure S7. The first charging process of Zn/NiMnHCF cell, 20 mA • g^{-1}, 1-1.85 V (V *vs*. Zn^{2+}/Zn), and corresponding *operando* PXRD measurement results of the specific points

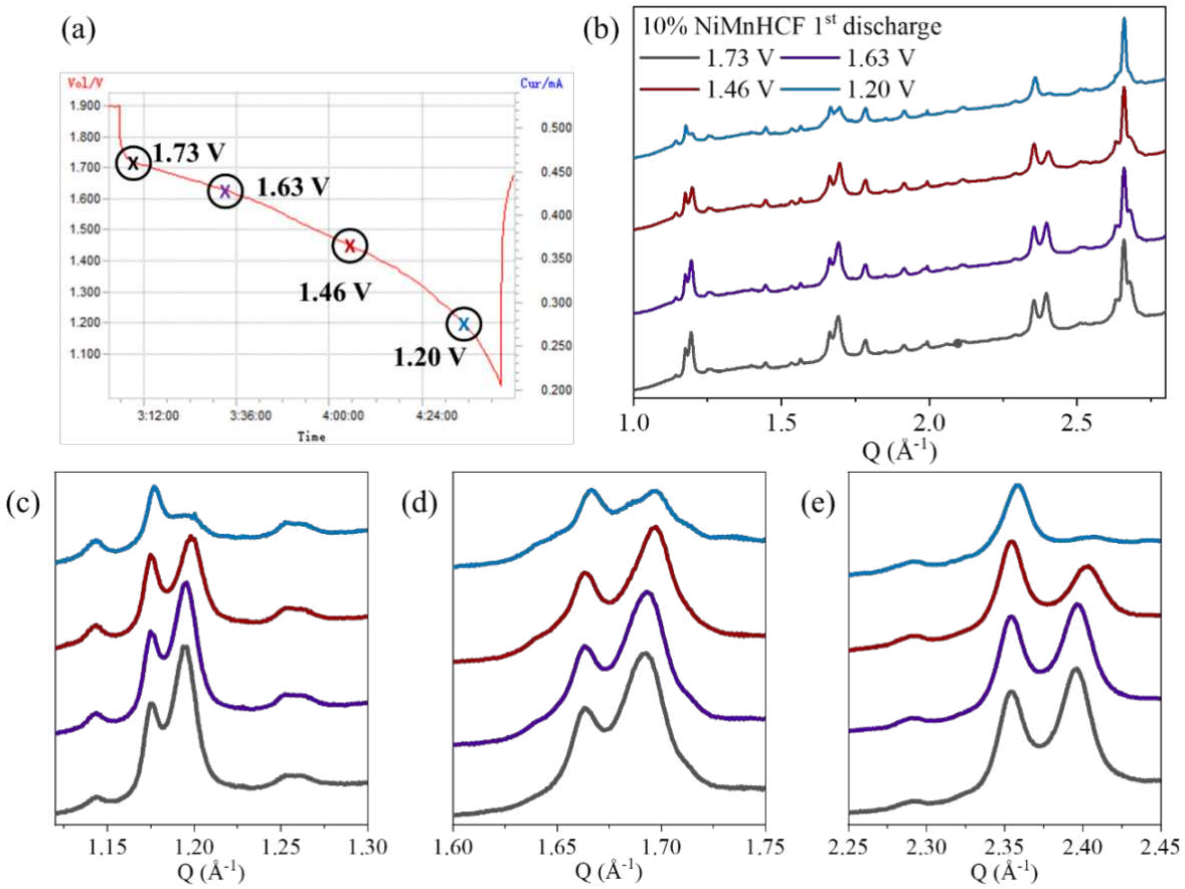

Figure S8. The first discharging process of Zn/NiMnHCF cell, 20 mA • g^{-1}, 1-1.85 V (V *vs*. Zn^{2+}/Zn), and corresponding *operando* PXRD measurement results of the specific points

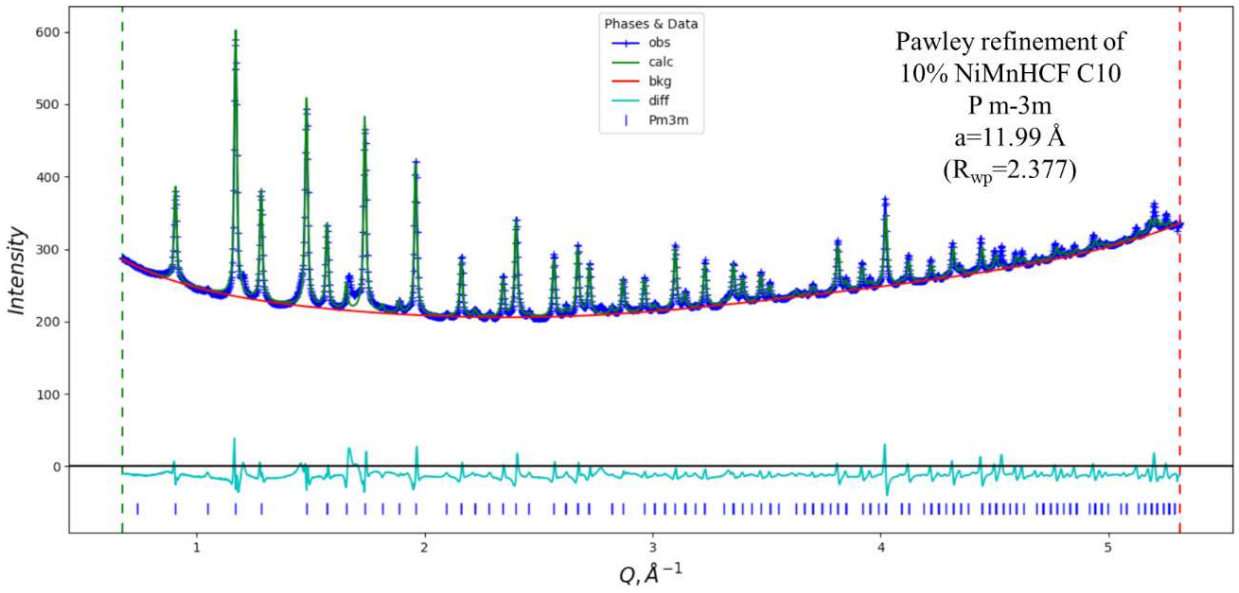

Figure S9. The Pawley refinement of NiMnHCF C10 sample with P m-3m phase

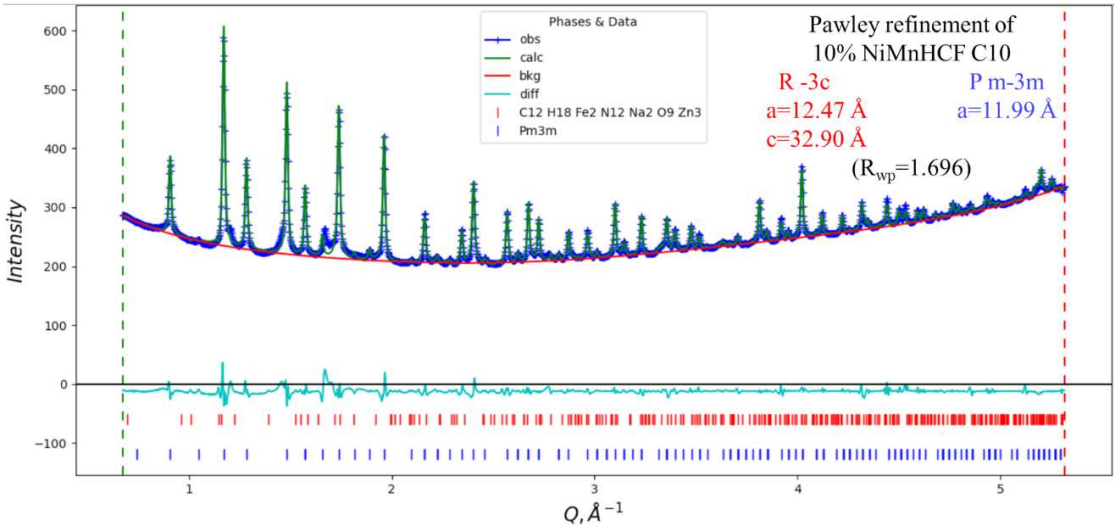

Figure S10. The Pawley refinement of NiMnHCF C10 sample with P m-3m and R -3c phases

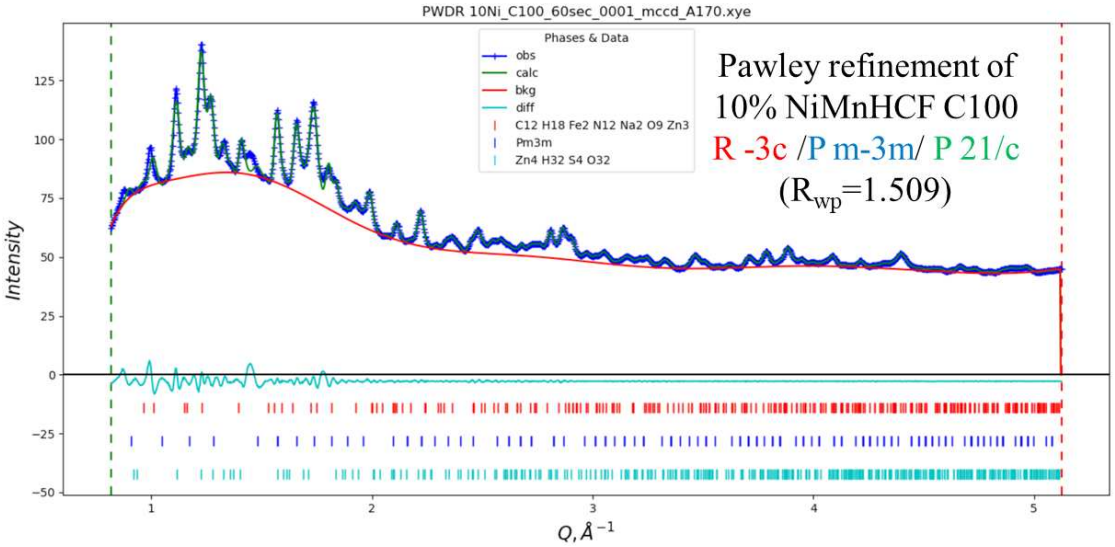

Figure S11. The Pawley refinement of NiMnHCF C100 sample with P m-3m, R -3c and P 21/c phases

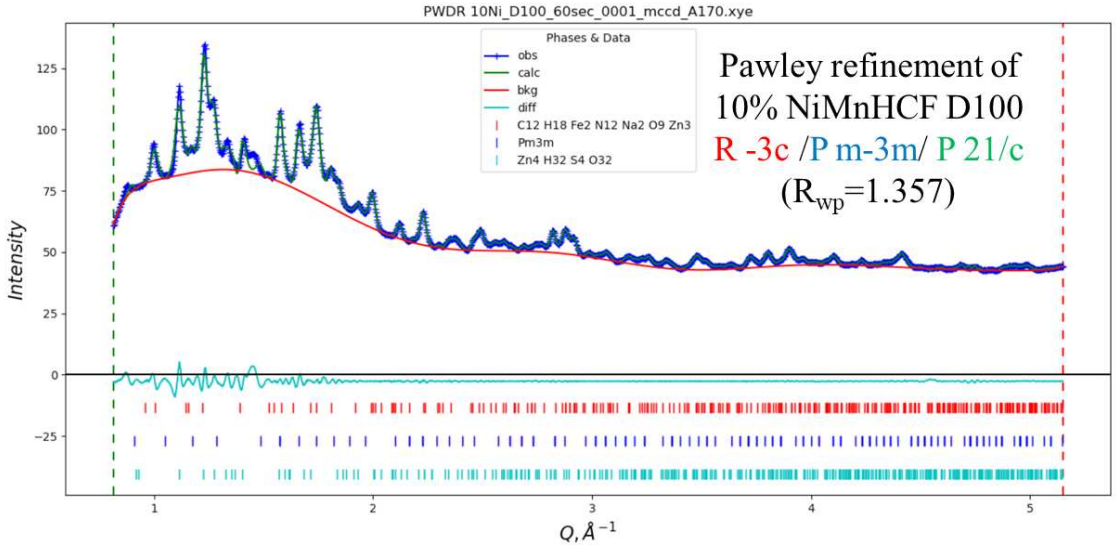

Figure S12. The Pawley refinement of NiMnHCF D100 sample with P m-3m, R -3c and P 21/c phases